INVITED REVIEW

Journal of Microscopy | RMS

Current opinion on the prospect of mapping electronic orbitals in the transmission electron microscope: State of the art, challenges and perspectives

M. Bugnet[1,2,3] ⓘ | **S. Löffler[4]** ⓘ | **M. Ederer[4]** ⓘ | **D. M. Kepaptsoglou[2,5]** ⓘ |
Q. M. Ramasse[2,3,6] ⓘ

[1]CNRS, INSA Lyon, Université Claude Bernard Lyon 1, MATEIS, UMR 5510, Villeurbanne, France

[2]SuperSTEM Laboratory, SciTech Daresbury Campus, Daresbury, UK

[3]School of Chemical and Process Engineering, University of Leeds, Leeds, UK

[4]University Service Centre for Transmission Electron Microscopy, TU Wien, Wien, Austria

[5]School of Physics, Engineering and Technology, University of York, York, UK

[6]School of Physics and Astronomy, University of Leeds, Leeds, UK

Correspondence
M. Bugnet, CNRS, INSA Lyon, Université Claude Bernard Lyon 1, MATEIS, UMR 5510, 7. avenue J. Capelle, Villeurbanne 69621, France.
Email: matthieu.bugnet@insa-lyon.fr

S. Löffler, University Service Centre for Transmission Electron Microscopy, TU Wien, Stadionallee 2, Wien 1020, Austria.
Email: stefan.loeffler@tuwien.ac.at

Abstract

The concept of electronic orbitals has enabled the understanding of a wide range of physical and chemical properties of solids through the definition of, for example, chemical bonding between atoms. In the transmission electron microscope, which is one of the most used and powerful analytical tools for high-spatial-resolution analysis of solids, the accessible quantity is the local distribution of electronic states. However, the interpretation of electronic state maps at atomic resolution in terms of electronic orbitals is far from obvious, not always possible, and often remains a major hurdle preventing a better understanding of the properties of the system of interest. In this review, the current state of the art of the experimental aspects for electronic state mapping and its interpretation as electronic orbitals is presented, considering approaches that rely on elastic and inelastic scattering, in real and reciprocal spaces. This work goes beyond resolving spectral variations between adjacent atomic columns, as it aims at providing deeper information about, for example, the spatial or momentum distributions of the states involved. The advantages and disadvantages of existing experimental approaches are discussed, while the challenges to overcome and future perspectives are explored in an effort to establish the current state of knowledge in this field. The aims of this review are also to foster the interest of the scientific community and to trigger a global

effort to further enhance the current analytical capabilities of transmission electron microscopy for chemical bonding and electronic structure analysis.

1 | INTRODUCTION

Electronic states underpin most chemical and physical properties of solids, defining their electronic structure and reactivity, as well as their optical, magnetic, and transport characteristics of interest for a wide range of applications. Specifically, among all electronic states of atoms constitutive of a material, those forming electronic orbitals responsible for chemical bonding are of fundamental interest to understand the intrinsic properties of interfaces and defects. For instance, chemical bond formation between atoms during chemical reactions is driven by energy considerations, and takes place preferentially at nucleation sites like crystal discontinuities (e.g., surface steps, kinks, etc.) for, for example, heterogeneous catalysis[1] or thin film growth.[2] Electronic, optical, and transport properties of crystals are affected – and sometimes fully driven – by the presence of point defects such as vacancies, interstitial or substitutional atoms.[3–5] The response of materials to a mechanical stress is different for a single crystal and a polycrystal, as it is determined by the presence of crystal discontinuities like grain boundaries and interfaces, and can manifest itself by the creation of extended defects like dislocations.[6] Therefore, mapping electronic states specifically at crystal discontinuities would be of importance and is thus far essentially lacking. It is also noteworthy that the direct observation of electronic states, irrespective of their interpretation as electronic orbitals, remains extremely elusive even in the bulk of materials.

Total electron densities have been retrieved for decades from X-ray, neutron and electron elastic scattering experiments. However, this is usually obtained without momentum selectivity, which is necessary to distinguish between orbitals and therefore to properly describe chemical bonding. Nevertheless, non-resonant X-ray inelastic scattering was employed to successfully plot the contour of the Ni^{2+} $3d$ x^2-y^2/$3z^2$-r^2 orbital in single crystal NiO,[7] while the difference of two-dimensional (2D) electron momentum densities between $LiFePO_4$ and $FePO_4$ probed by X-ray Compton scattering is theoretically expected to provide the wave function of the redox orbital.[8] In the transmission electron microscope, total electron densities have been

mapped at the atomic scale, by convergent beam electron diffraction (CBED),[9,10] high-resolution transmission electron microscopy (HRTEM),[11] and more recently four-dimensional scanning transmission electron microscopy (4D-STEM).[12–15] These methods, whether performed in real or reciprocal space, rely almost exclusively on elastic signals, which only give direct access to the total atomic charge density, irrespective of individual electronic states of interest for chemical bonding. This elastic approach alone cannot show the required chemical specificity or sensitivity to directly interpret the properties linked to particular valence electrons associated with chemical bonding. Orbital information can be extracted indirectly when these techniques are combined with the appropriate additional input. Specifically, this is the case of the work of Zuo et al.[9] on Cu_2O, in which the difference between the static crystal charge density obtained from convergent beam electron diffraction (CBED) and the calculated charge density of spherical O^{2-} and Cu^+ ions lead to a d_{z^2} shape around the Cu atom, which was interpreted as a clear indication of a covalent bonding component.

Several other experimental techniques have been employed to 'measure' electronic orbitals directly and retrieve orbital maps.[16] Originally, they were developed for imaging orbital densities in molecules, in the quest towards monitoring orbital changes during chemical reactions. This is the case of high harmonic generation[17,18] electron momentum spectroscopy,[19] angle resolved X-ray photoemission spectroscopy[20] and scanning tunnelling microscopy (STM).[21–23]

Given the spatial distribution of electronic states, techniques allowing sub-Å resolution like scanning probe microscopies and transmission electron microscopy appear best-suited for direct visualisation of orbitals. STM appears as a powerful surface microscopy technique for mapping complex molecular orbital configurations, particularly at cryogenic temperatures on inert substrates. STM enabled the pioneering visualisation of the lowest unoccupied and highest occupied molecular orbitals in large molecules adsorbed at solid surfaces, such as pentacene[21,22] and naphtalocyanine.[23] However, this technique is intrinsically limited by its surface sensitivity
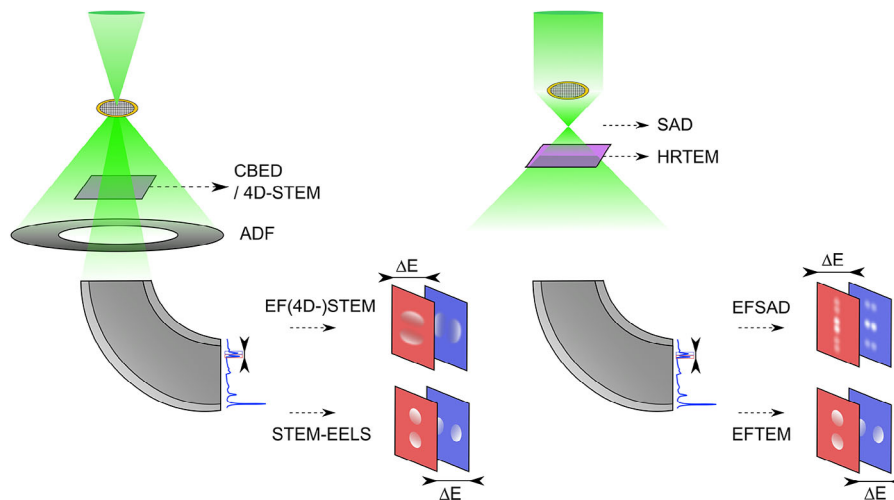
FIGURE 1   Schematic representation of several techniques accessible in modern TEM instruments for mapping the atomic charge density or individual electronic states: with a focused electron probe (left) (convergent beam electron diffraction, CBED; four-dimensional scanning transmission electron microscopy, 4D-STEM; STEM-electron energy-loss spectroscopy, STEM-EELS; energy-filtered 4D-STEM, EF-4D-STEM), and parallel electron beam (right) (high-resolution TEM, HRTEM; selected area diffraction, SAD; energy-filtered TEM, EFTEM; energy-filtered SAD, EFSAD). The signals in EF(4D-)STEM and EFSAD are smeared to represent the convolution with a Lorentzian (see Section 3.2 for details).

and is thus oblivious to electronic states in the bulk of materials.

Following the development of aberration correctors for electromagnetic lenses, high brightness electron guns, and high stability electron-optics in STEM since the early 2000s, electron energy-loss spectroscopy (EELS) has become routinely available for atomic resolution analysis of a wide range of crystals. EELS is an absorption spectroscopy probing site- and momentum-projected empty states in the conduction band,[24,25] which can be associated to anti-bonding orbitals, and has led to elemental mapping[26–28] and detecting variations of the spectral fine structure[29–37] – or energy-loss near edge structure (ELNES) – at the scale of a single atomic column or plane.

Therefore, combining the inelastic signal at EELS absorption edges and the elastic signal from imaging or diffraction with a sub-Å highly focused probe in STEM has the potential to produce real-space visualisation of (antibonding) electronic orbitals at the atomic scale.[38] Following this approach, STEM-EELS was employed to map orbitals in real space in bulk TiO_2[39] and in epitaxial graphene multilayers.[40]

In this review, the current state-of-the-art of electronic orbital visualisation in solids in the transmission electron microscope is presented with a critical point of view. The distinction between elastic and inelastic scattering is considered, with approaches in real and reciprocal spaces in both STEM and TEM (see Figure 1), and their ability to provide electronic charge density maps or orbital maps at the atomic-scale is discussed. Current challenges to address

and perspectives for orbital mapping in the transmission electron microscope are discussed in the final section.

2 | ELASTIC SCATTERING

2.1 | Real space

Visualising electronic charge density fluctuations, like charge transfer, at the level of a single atom, for instance on a single point defect is extremely challenging from diffraction experiments. Using elastic scattering as in HRTEM imaging provides an alternative way to map the electronic configuration of such defects.

Meyer et al.[11] have demonstrated that insights into the charge distribution at the single atom level could be obtained from accurate and well-controlled HRTEM experiments. The charge transfer at single N-substitution point defects in graphene was confirmed from the experimental contrast obtained at well-controlled defocus value and its agreement with image simulations based on density functional theory (DFT) (see Figure 2A and B). The contrast of the N-substitution defect is shown to be primarily due to a change in the electronic configuration on the neighbouring carbon atoms. In a second two-dimensional material, namely, single-layer and double-layer h-BN, the experimental intensity of B- and N- atoms in the HRTEM image is nearly identical, and only well reproduced by DFT contrary to an independent atom model (see Figure 2C and D). This loss of elemental contrast, well reproduced by DFT, is due to the electronic charge redistribution. The
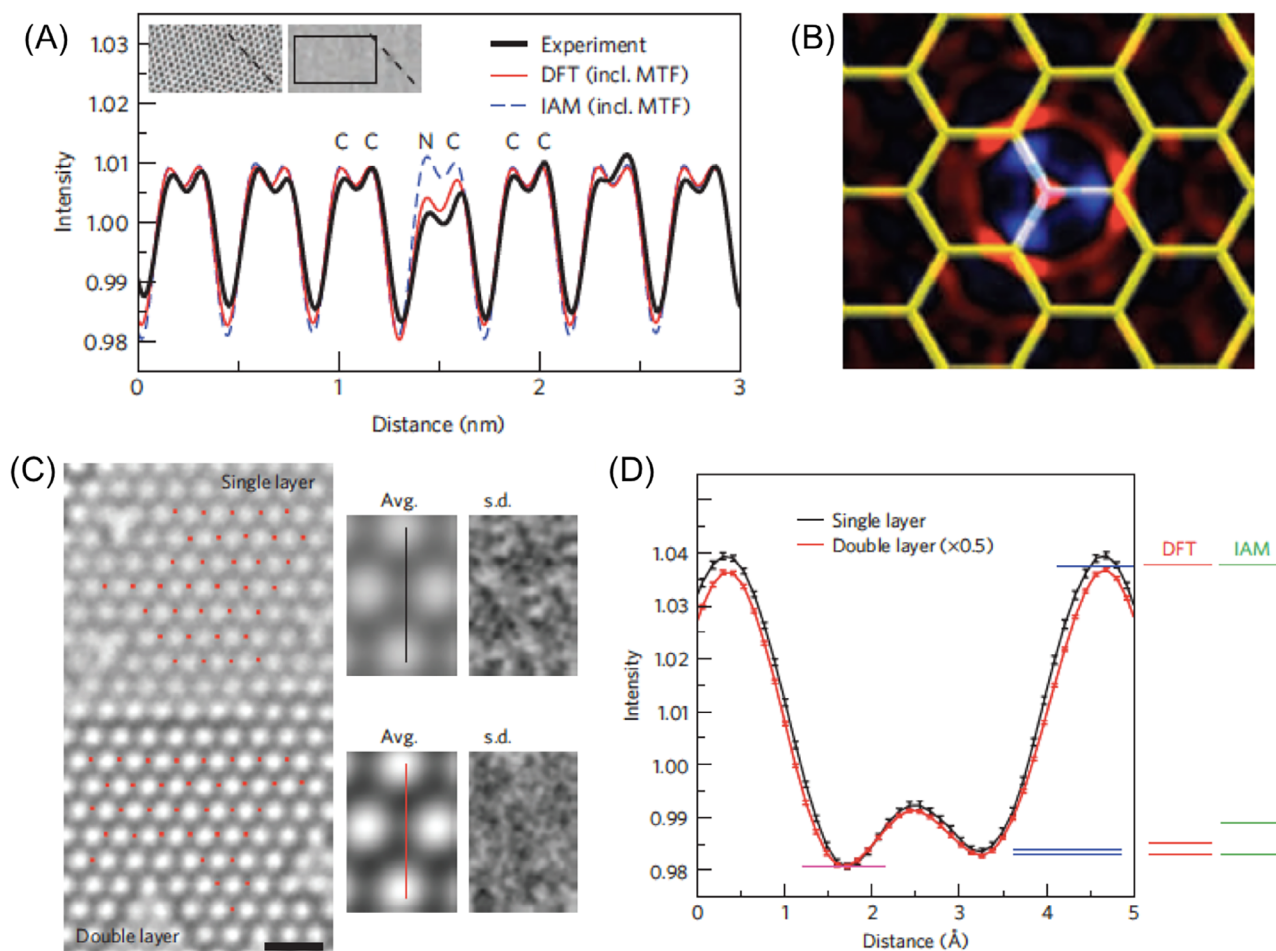
FIGURE 2 (A), (B) Nitrogen substitution defect in graphene. (A) Comparison between experiment and simulations based on the independent atom model (IAM) and DFT potentials. MTF: modulation transfer function. Inset: The image and profile, and the Fourier-filtered image (graphene lattice removed). (B) Effect of bonding on the projected electron density (blue (red) = lower (higher) electron density in the DFT result as compared with the independent atom model. The atomic structure is overlaid. (C), (D) h-BN. (C) HRTEM of single- and bi-layer h-BN (scale bar: 5 Å). The unit cells chosen for analysis are indicated by the red dots. (D) Intensity profiles from the single- and double-layer average with standard deviation as error bars. The contrast of the double layer was reduced by a factor of 2 and the intensity minimum on the left sublattice was shifted to the same value as for the single layer (pink line), enabling the comparison between the intensity minima on the right sublattice (blue lines). The contrast difference between single and double layer h-BN determined from IAM and DFT model is indicated on the right. Reprinted with permission from Meyer et al.,[11] Nature Publishing Group.

experimental contrast and its agreement with DFT confirms the ionic character of single-layer h-BN. This work also emphasised that the independent atom model was not sufficient to explain the charge redistribution-induced contrast variations in HRTEM images, and that simulations including electronic structure component such as DFT, were required for proper interpretation.

2.2 | Reciprocal space

Experimental approaches based on electron diffraction, like CBED in static or scanning (4D-STEM) configurations, have led to mapping total electron densities of atomic species at the atomic scale. Such approaches were per-

formed in a wide range of materials,[15] including metals,[10] semiconductors,[14] and ceramics like metal oxides.[9,12,13] While total electron densities do not directly reflect orbital configurations in a crystal, Zuo et al.[9] have demonstrated that orbital information could be retrieved in Cu_2O (cuprite) through a quantitative approach involving the precise determination of CBED intensity and atomistic calculations. Specifically, this approach consists in mapping the difference between the static crystal charge density and the superimposed charge density of spherical O^{2-} and Cu^+ ions. The former was obtained from the multipole fitting to the experimental intensity profiles across CBED disks, as shown in Figure 3A, while the latter was calculated by the multi-configuration Dirac-Fock method. The resulting contrast in the electron density difference maps
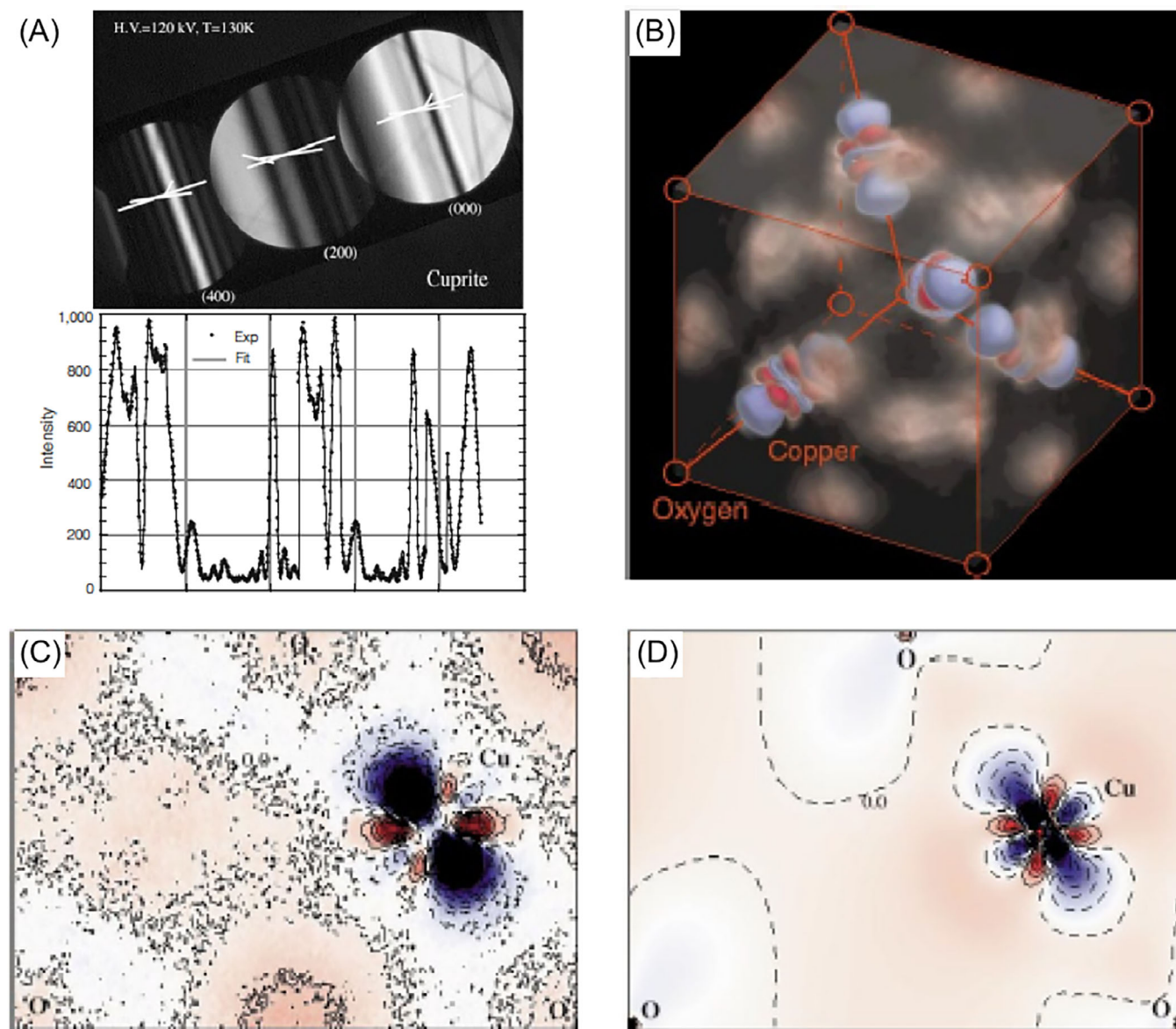
FIGURE 3 (A) top: experimentally recorded and processed CBED pattern for Cu_2O; bottom: best fit for electron diffraction structure factor measurement of Cu_2O (200) and (400) for points along lines indicated in top, displayed sequentially along the *x*-axis and with the recorded intensity on the *y*-axis in counts. (B) A three-dimensional rendering of the experimental difference map from the multipole model fitting with anharmonic temperature factors. The map was made using a colour scheme of blue ($\Delta\rho < 0$), white ($\Delta\rho = 0$) and red ($\Delta\rho > 0$). A translucency factor was used to remove the mostly white background. (C) Contour map of the difference charge density in a (110) plane with a contour increment of 0.2 electrons per $Å^2$ and coloured using the same colour scheme as in (B). The dashed line is for contours with $\Delta\rho \leq 0$. (D) The difference charge density map obtained from the FLAPW (LDA) calculations, plotted in the same way as (C). Reprinted with permission from Zuo et al.,[9] Nature Publishing Group.

shows a non-spherical charge density around Cu atoms and a clear d_z^2 orbital shape (Figure 3B–D). This charge distribution was unexpected for a purely ionic bonding, thereby demonstrating unambiguously a covalent bonding contribution.

This example shows that quantitative CBED offers a path to determine the degree of covalence in iono-covalent systems by reconstructing orbital density. While this approach provided an experimental solution to a

scientific mystery for Cu_2O, it also has drawbacks. In the static configuration, that is, when a single CBED pattern is taken with the electron beam fixed on the sample, this method suffers from the lack of intrinsic spatial resolution, and is limited to the bulk part of materials. Coupled to 4D-STEM, that is, the recording of multiple CBED patterns by the scanning electron beam with sub-Å displacement, this quantitative approach would allow defects and interfaces to be probed distinctively from the

bulk. In Cu_2O, quantitative CBED provides an indirect path to retrieve individual Cu d orbital density distribution in real space, and its reliability depends strongly on the quality of the fit to CBED intensity variations and on the subtraction of a theoretical cationic charge density map obtained from atomistic calculations. The reliability of the atomistic calculations, that is, the degree of reproduction of the true electronic structure of the material, is thus an essential parameter to extract orbital contrast.

3 | INELASTIC SCATTERING

3.1 | Real space

EELS in the transmission electron microscope is a powerful technique to spectrally distinguish electronic states with different symmetries from core-level excitation at atomic resolution. Therefore EELS appears well-suited to fulfil the objective of visualising directly, that is, in real space, specific electronic transitions to unoccupied states, that is, antibonding orbitals. Contrary to the well-established STEM-EELS approach in which the beam is used as a raster on the specimen while a real-space image and spectral information are recorded, keeping the atomic scale information in reciprocal space while using EELS poses various experimental challenges. This point is discussed in Section 4.

STEM-EELS was applied to rutile TiO_2 [001], providing the first direct view of individual electronic orbital contrast in energy-filtered STEM-EELS maps.[39] As shown in Figure 4, the experimental energy-filtered map for the e_g final states of the $Ti-L_{23}$ edges shows a clear elongation of the contrast centred on each Ti atomic column, along the direction of the nearest O columns. The contrast is also rotated 90° from one Ti atomic column to the next. This elongation confirms the prediction from calculated maps, obtained using the mixed dynamic form factor approach and considering a DFT-established electronic structure of TiO_2 for the inelastic event, and the multislice algorithm for the electron propagation through the specimen thickness. Considering an independent atomic model, this elongation is lost, thus confirming the experimental visualisation of atomic orbitals with e_g character. This study is a proof of principle that electronic orbitals can be mapped directly, that is, in real space, using STEM-EELS in currently available microscopes, provided that the spherical aberrations of the condenser lenses are corrected and the stability of the instrument is optimised.

A similar approach was employed more recently in the case of epitaxial graphene multilayers.[40] The π^* orbitals are delocalised out of the graphene planes, as highlighted in Figure 5A where the orbital lobes clearly stick out-of-plane. This geometrical specificity suggests that π^* orbitals could be visualised when graphene is observed in side view, that is, for an incident electron beam located within the graphene sheet. The experimental contrast in π^*, σ^*, and π^*/σ^* maps (see Figure 5B), however, shows that their interpretation is much more complex. Simulations including both inelastic scattering and channelling effects were necessary to interpret the experimental maps, as shown in Figure 5D. The accurate reproduction of the atomic-scale π^*/σ^* signal variations (Figure 5F) by such calculations demonstrates that the contrast in the experimental maps actually comes from the π^* and σ^* orbitals of interest, modulated by channelling and geometrical effects of the probe.

A theoretical study on point defects like N-substitution and vacancy in graphene suggests that atomic orbitals could be mapped using a convergent beam as in STEM-EELS, but also with a parallel-beam illumination in so-called energy-filtered TEM (EFTEM) experiments.[41] EFTEM on the atomic scale has been attempted over the past decade; however, thus far only elemental mapping at atomic resolution has been demonstrated.[42–44] In practice, EFTEM showed insufficient signal and spatial resolution to extract maps of individual electronic transition probabilities, that is, fine structure EFTEM maps at the atomic scale. The signal and noise levels remain particularly challenging to overcome in EFTEM, which also requires chromatic aberration correction of the objective lens to ensure elemental mapping in the EELS spectrum while maintaining atomic scale resolution.[45]

3.2 | Reciprocal space

In addition to mapping the real-space distribution of electronic transitions, one can also map their momentum distribution. Actually, using EELS in reciprocal space to map momentum information of transitions to individual orbitals predates the real-space mappings, which is likely due to the less stringent requirements on spatial resolution and stability when using a parallel beam.

As is typical in classical diffraction, a parallel beam is used to ensure as little blurring as possible due to a large range of incident angles contributing to the final pattern. Like in the real-space case, the selection of a narrow energy range in the core-loss region is typically required to ensure only transitions to a single or a select few final states contribute to the data. Finally, one or more energy-filtered diffraction patterns are recorded and analysed. To enable, for example, background subtraction, multiple datasets (or, ideally, a whole data cube) need to be recorded. This
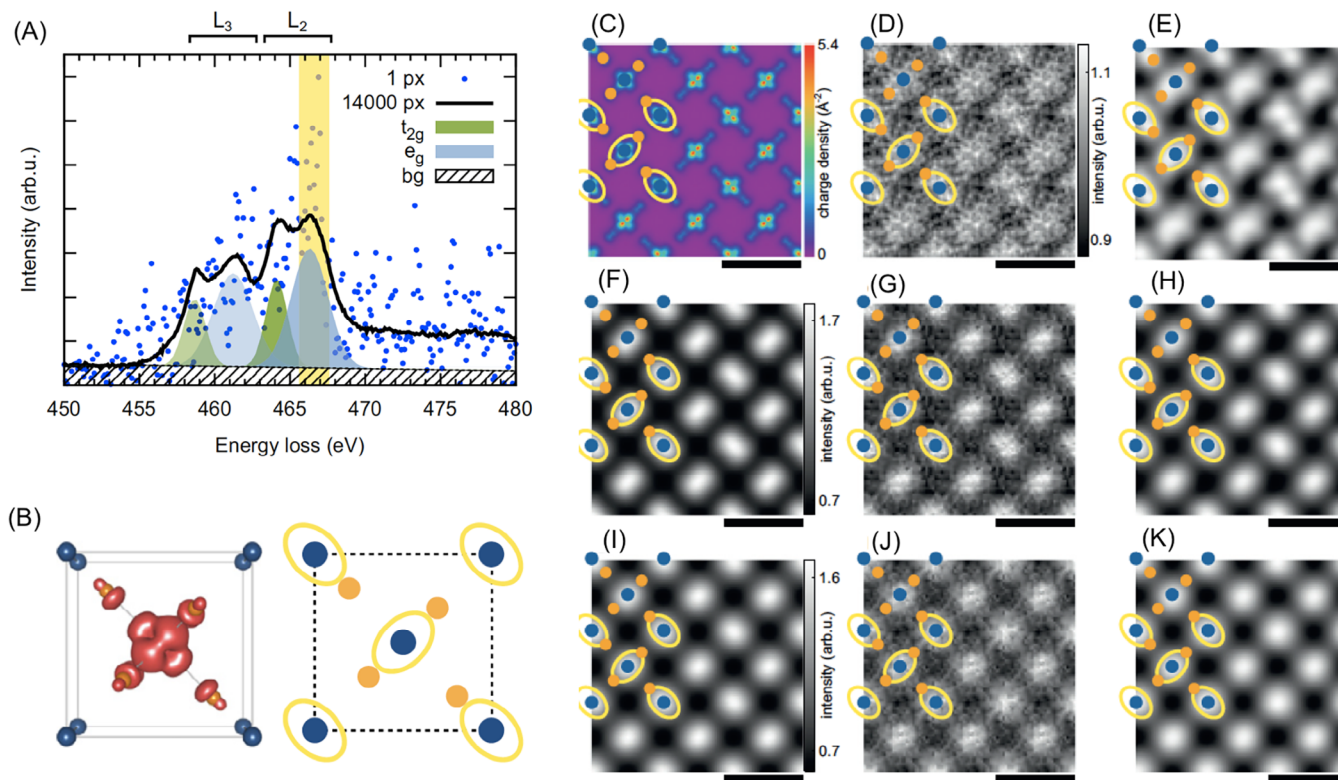
FIGURE 4 (A) $Ti - L_{2,3}$ edge extracted from a single pixel (dots), and averaged over all 14,000 pixels (line) of the data set. The energy window used for the energy-filtered e_g maps is highlighted in yellow. Gaussian least squares fits representing the individual shapes of the e_g and t_{2g} contributions are depicted in blue and green. (B) Unit cell along the [0 0 1] direction used in the experiment with the summed three-dimensional charge density of the e_g Wannier functions. Also shown are the projected positions of Ti (blue) and O (orange) atoms as well as yellow ellipses indicating the nearest O neighbours of each Ti (due to the projection, only two of the four nearest neighbours are visible). (C) Charge density for the unoccupied e_g orbitals projected along the [0 0 1] crystallographic axis as calculated by WIEN2k. (D) Experimental energy-filtered map for the Ti L ionisation edge for final states with e_g character after unit-cell averaging. (E) Same as (D), but after Gaussian smoothing. (F) Simulated energy-filtered map using the multislice algorithm and the MDFF approach after Gaussian blurring. (G) Same as (F) with added noise to better mimic the experimental conditions. (H) Same as (G) after Gaussian smoothing. (I)–(K) Same as (F)–(H) assuming independent atoms without bonding. All maps are replicated in a 3×3 raster for better visibility. Overlays show the projected positions of Ti (blue) and O (orange) atoms as well as yellow ellipses indicating the nearest O neighbours of each Ti (due to the projection, only two of the four nearest neighbours are visible). All scale bars indicate 5 Å. (For interpretation of the references to colour in this figure legend, the reader is referred to the web version of this article.) Reproduced with permission from Löffler et al.,[39] Elsevier.

is typically achieved either by putting the spectrometer in EFTEM mode and acquiring energy-filtered diffraction patterns at multiple energy losses, or by putting the spectrometer in a mode adapted to band-structure mapping, so-called ω-q-mode, and acquiring multiple stripes across the diffraction pattern.

Due to the long-range Coulomb interaction, a large range of momentum transfers is possible in inelastic (core-loss) scattering. In many cases, this is approximated by a Lorentzian distribution, which works well for small angle scattering ($\theta \ll \theta_B$ with θ_B being the Bragg angle) but fails for medium to large scattering angles, as this assumed Lorentzian shape arises from a (truncated) small-angle Taylor expansion of the scattering kernel.[46] This limitation is immediately obvious when one considers the fact that the integral over a Lorentzian distribution in a 2D plane

(i.e., over all scattered intensity in the diffraction plane) diverges. From an impact parameter perspective, electrons passing close to the atom, that is, at small impact parameter, are scattered to large angles, while those passing far from the atom, that is, at large impact parameter, get scattered to small angles. Therefore, orbitals will mostly affect the former, that is electrons passing in close proximity, and not so much the latter, that is electrons passing far away. As a result, deviations from the 'usual' Lorentzian, which we attribute to the influence of the orbitals, occur at larger scattering angles. More details about the description of Lorentzian inelastic scattering distribution can be found in the work of Löffler et al.[46] who linked the deviations from the Lorentzian distribution directly to the radial wavefunctions of the contributing orbitals (see Figure 6A and B).
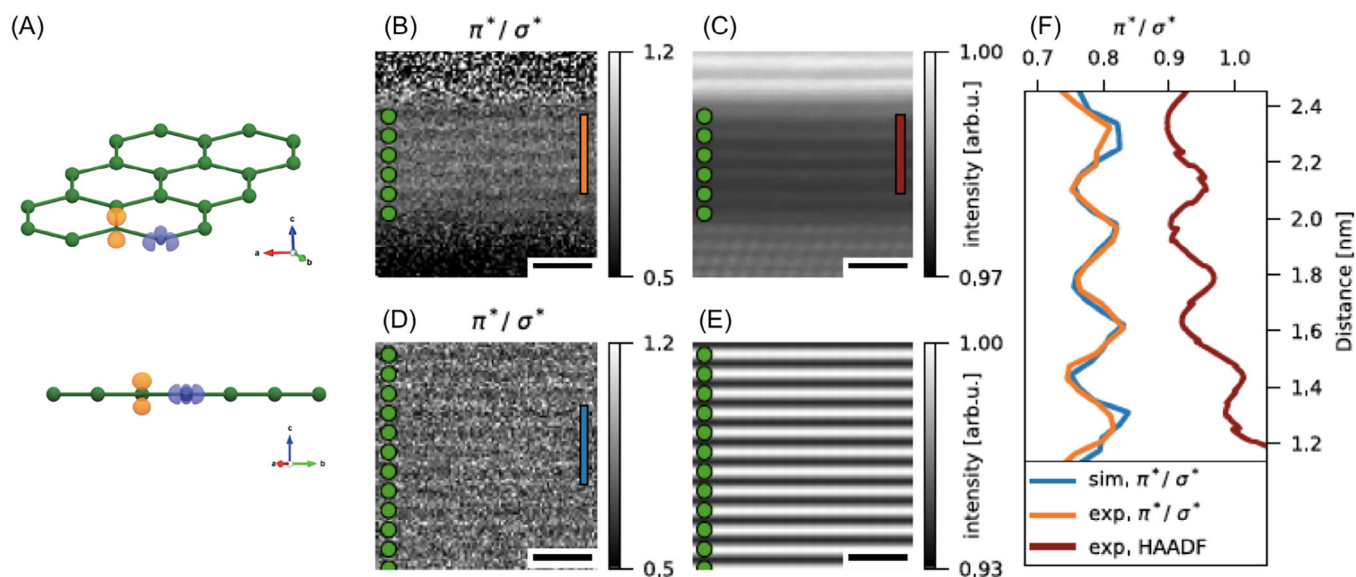
FIGURE 5 (A) Structural model of graphene and superimposed schematic representation of π^* (orange) and σ^* (blue) electron densities obtained from density functional theory. The inelastic channelling calculations were performed with the graphite layers oriented in the [10$\bar{1}$0] zone axis, as shown at the bottom. (B) Experimental π^*/σ^* maps and (C) HAADF image. (D) Theoretical π^*/σ^* maps with shot noise and (E) HAADF image. The position of atomic planes from the HAADF signal is indicated with green circles. (F) π^*/σ^* profiles from (B, D), and HAADF intensity integrated in the range indicated by the vertical orange, blue, and red bars in (B), (C), and (D). All scale bars indicate 1 nm. Reproduced with permission from Bugnet et al.,[40] American Physical Society.

In addition to the information about the radial distribution of the contributing orbitals, the momentum distribution of the inelastically scattered electrons also contains directional information about the contributing orbitals. This can easily be understood by considering the fact that each orbital has a specific momentum distribution associated with it. Hence, some momentum transfers between the beam and the sample are more likely than others, depending on the orientation of the orbitals. This effect has been exploited in materials with high bonding anisotropy, for example, graphite[49–52] where the inelastic scattering distribution of transitions to π^* and σ^* states are distinguishably different from one another,[47] as shown in Figure 6C–F. More recently, Fossard et al.[48] mapped the π^* and σ^* momentum distributions in h-BN with high resolution in momentum space, as illustrated in Figure 6G–J.

One could argue that reciprocal-space mapping – at least when employing a parallel incident beam – is not 'real' mapping of transitions between *individual* orbitals as such measurements inherently average over a large area. However, when a single crystalline sample with homogenous thickness is used, all unit cells are arguably identical. In that sense, there is no difference between averaging over many unit cells by illuminating a large area in the reciprocal-space approach and averaging over many unit cells in postprocessing as is currently necessary in the real-space approach to reach an acceptable signal-to-noise ratio (SNR). Of course, using a large, parallel beam necessitates

an excellent sample, while averaging in real space requires excellent beam and sample stability.

Whether real-space or reciprocal-space mapping is easier to achieve, and whether real-space or reciprocal-space information is more suitable for answering a given research question, needs to be determined on a case-by-case basis. Currently, real-space mapping seems more promising for answering application-relevant questions often revolving around electronic states at defects and interfaces, while reciprocal-space mapping might be more suitable for fundamental research and understanding general material properties. However, there may also be merit in employing 4D-STEM to get the best of both worlds as discussed below.

4 | DISCUSSION

Mapping orbital information is currently right at the edge of what is possible with the latest generation of electron microscopes. However, there are many challenges and confounding factors that need to be understood, analysed carefully and hopefully overcome on a case-by-case basis in order to produce meaningful, reproducible results.

The first and maybe most fundamental and controversial aspect is the question of what properties are actually measurable. While 'mapping orbitals' is a nice catch phrase that is used throughout the literature relatively loosely,
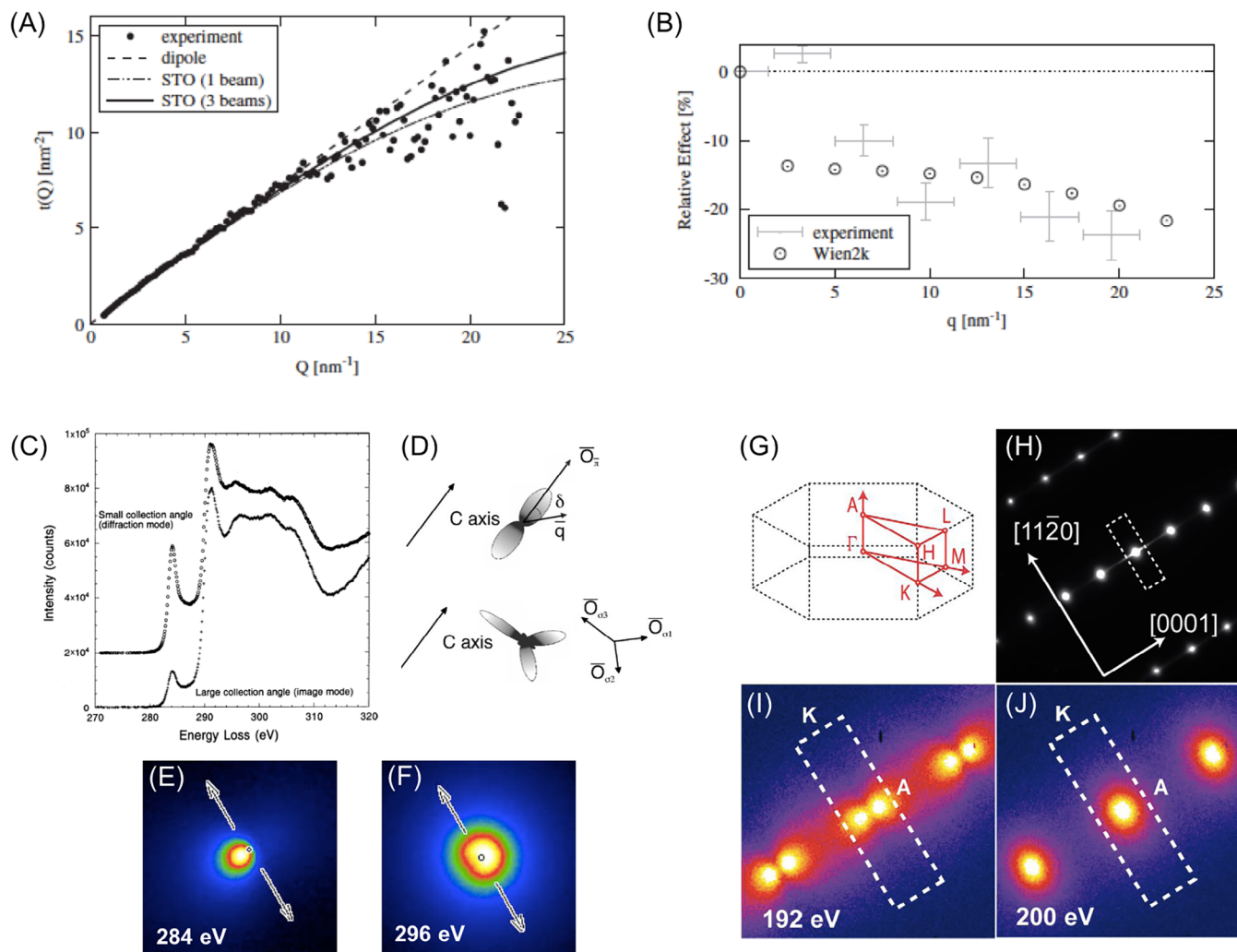
FIGURE 6 (A) $Q^2\sqrt{I(Q,E)/I(q_E,E)}$ as calculated by Slater-type orbitals using one beam (no elastic scattering) and three beams (with elastic scattering) for Si. The curves are superimposed on experimental data. The dashed line shows the dipole approximation. (B) WIEN2k simulations of the relative deviations from the Lorentzian, superimposed on the experimental data for Si. These calculations include a proper treatment of the energy dependence, but no elastic scattering. Reproduced with permission from Löffler et al.,[46] Elsevier. (C) EELS C-K edges of graphite showing the expected anisotropy of the near-edge structure as demonstrated in two angular collection conditions. (D) Representation of the orientation of the $\pi*$ (top) and $\sigma*$ orbitals (bottom) in the crystals. There are three equivalent $\sigma*$ orbitals joining C atoms in the graphene sheet. The vector $\vec{O}$ represents the direction of maximum amplitude of the orbital. δ represents the angle between the scattering vector $\vec{q}$ and the vector $\vec{O}$. (E), (F) Details of the energy filtered patterns obtained with the sample oriented with the c-axis at 45° with the electron beam, for windows at 284 eV and 296 eV, respectively, after subtraction of the 270 eV scattered intensity. The patterns show the location of the forward scattering direction of the incident beam (the small circle) and the axis of rotation of the sample (arrow) by the angle γ. The c-axis projection lies perpendicular to the rotation axis. Reproduced with permission from Botton,[47] Elsevier. (G) Hexagonal Brillouin zone and (H) diffraction pattern of h-BN in a plane containing the hexagonal axis (direction Γ A) and the Γ K direction. (I), (J) Energy-filtered scattering patterns recorded at 192 eV and at 200 eV, respectively. Reproduced with permission from Fossard et al.,[48] American Physical Society.

quantum mechanics dictates that it is impossible to measure a single quantum state in isolation. Every measurement always perturbs the measured object, so one is always measuring transitions between different states. Nevertheless, the disturbance may be very small, as assumed in the case of elastic scattering on a 'rigid' charge density, or one may have prior knowledge about one of the contributing states (e.g., the tightly bound ground state, which is mostly unaffected by the surroundings of the atom and, therefore, well described by theory).

In the case of elastic scattering (Section 2), the dominant process is scattering on the Coulomb potential. No internal degrees of freedom are considered other than, potentially, phonon excitations, and the result is information about the total charge density. While this does not give information about individual electronic states

but rather about the (incoherent) sum over all electronic states superimposed on the effect of the nuclear potential, it can provide valuable insights, particular into deviations from the perfect crystal, for example, in the vicinity of defects.

In the case of inelastic scattering (core-loss EELS, Section 3), the dominant process is the excitation of a sample electron from a tightly bound initial state to a final conduction state. In this case, transition probabilities can be determined based on the prepared initial beam state and the measured final beam state(s). Nevertheless, with prior knowledge about the sample's initial state, much information can be gained about the final state(s). As a simple example, consider a K-edge excitation. It is known that the sample's initial state has s symmetry, that is, it is spherically symmetric. Therefore, any deviation from circular symmetry in the inelastic image (or diffraction pattern) has to stem from the sample's final state (or the probe's states – such artefacts need to be avoided by careful planning of the experiment). Thus, with careful planning and execution of the experiments to avoid artefacts, and with prior knowledge about the sample's initial state, one can indeed gain information about the selected final states of a given transition, such as its spatial or momentum distribution. However, it is important to emphasise that all information is always 'filtered' through the sample's initial state and the contributing probe beam's states. If a transition to a certain final state is forbidden for a given choice of probe beam and initial sample state, for example, because it would violate some conservation law, no information about that final state can be obtained. Usually, in those cases, selecting a different initial sample state (i.e., a different excitation edge) or a different probe beam (e.g., moving it, tilting it or using beam shaping techniques) can overcome such issues.

Regarding experiments, the first and perhaps most obvious challenge is the low SNR. This is inherent to the method, as narrow energy windows much smaller than those typically used for regular chemical mapping are required to pick out transitions to the specific final states one wants to measure. As of yet, there is no universal way to overcome this issue, other than to optimise all available experimental parameters for the situation at hand. The maximum energy range is, of course, determined by the material and excitation edge of interest. Generally, a larger chemical splitting is beneficial as it allows for larger energy windows being usable. Increasing the incident beam's current can help, but in most cases, this would lead to a loss in spatial resolution and even damaging the sample. A larger sample thickness would also result in a larger core-loss EELS signal, albeit with more background as well, but thicknesses over a few nanometres are problematic in their own right and should generally be avoided as discussed below.

With the experimental conditions set, another aspect that can lead to improved SNR is better detectors. Here, the advent of direct detection could prove beneficial, as it circumvents read-out-noise completely, leaving an entirely shot-noise-limited signal. How large the improvement due to direct detection will be for orbital mapping remains to be seen, however. Due to the long-ranged Coulomb interaction and the fact that the probe beam is divergent past the focal point in STEM experiments, one practically never observes the pure signal of the transition to a single orbital, but rather always a mixture of the dominant signal coming from the position the beam is placed, with other signals stemming from neighbouring columns. As a result, one is rather looking at small changes between the relative signal intensities of various orbitals. In order to make out small changes on top of a large signal, one automatically needs high intensities even in the shot-noise-limited case (i.e., where noise is dominated by the large signal, not the small changes). By comparison, read-out noise is usually at least one order of magnitude smaller.

One additional possibility to overcome the SNR challenge is to use averaging, either by a large illuminated area as in reciprocal-space mapping, or by numerical postprocessing. This is the typical method used thus far. While it naturally poses problems when one wants to investigate point defects, it still is a viable method for line, area or volume defects as well as single crystals. In order to obtain meaningful results, it is important, however, to ensure that one is averaging identical areas, lest one mixes different signals.

The second experimental challenge is spatial resolution and stability. The typical length scales of the features under investigation – that is, the transition between tightly bound initial states and conduction states – are generally smaller than the interatomic distances of a few Å. In order to get at least a couple of different data points, one consequently needs a subresolution, preferably in the low tens of pm range.[1] While this is routinely achievable in state-of-the-art C_s-corrected microscopes in the elastic regime, with pixel dwell times on the order of μs, EELS maps typically require much longer exposure times per pixel on the order of ms or tens of ms. This is further exacerbated by the low SNR, which can lead to even longer exposure times. Naturally, both the sample and the beam should drift significantly less than one unit-cell over the time it takes to measure that unit cell. With $20 \times 20 \text{pixels}^2$ per unit cell, a lattice parameter of 5 Å, and a dwell time of 100 ms, this results in a drift $\ll 0.1$ Ås^{-1} to be sustained over minutes (to acquire multiple unit cells). Unfortunately, there currently is no easy solution for the stability problem, other than

---

[1] Measuring just 10 points over 5 Å without (significant) overlap requires a spatial resolution of 50 pm

ensuring excellent vibrational, thermal and electromagnetic stability throughout the measurement and possibly optimising detection efficiency to reduce overall measurement time.

The third challenge is channelling of the electron beam in the sample. This is caused by the elastic scattering in the sample atoms' Coulomb potential. It is present even in monolayer samples[11] and, therefore, has to be taken into account in data analysis and simulations. However, it gets much more pronounced with increasing sample thickness, to the point that channelling can be the dominant factor in determining which transitions are excited and which are not.[53–55] Thus, one has to resist the urge to use thicker samples, and therefore more scattering atoms in the beam path, to improve the overall signal strength as well as the SNR, in order to achieve interpretable results. Another reason to avoid thick samples is the required spatial resolution. In thick samples, not all planes can be in focus, particularly with the large convergence (and collection) angles required to reach the required spatial resolution and the resulting small depth of field. Since out-of-focus contributions do not contribute to the usable signal for the most part, the gain in raw counts due to increasing thickness is likely useless, thus actually reducing the SNR. The exact usable thickness range depends on several factors, including the sample atoms' scattering strengths, the incident dose, the orbitals under investigation, the accelerating voltage and the required level of accuracy, but a recent study found upper bounds in the range of 5 nm to 30 nm.[56]

The fourth challenge – or rather choice – is the choice of energies, that is, the ionisation edge and the high tension. Lower ionisation edge energies typically give stronger signals, which comes at the cost of lower spatial resolution due to the stronger delocalisation.[57] In the context of inelastic delocalisation, it must be noted that the scattering distribution is strongly peaked, with broad tails, as is common for the long-ranged Coulomb interaction.[58] The spatial resolution (on the scale of orbitals) is defined solely by the central peak of the scattering distribution, while the broad tails make up a substantial, but fairly homogeneous background. Therefore, common estimates for the delocalisation that are based on intensity alone (e.g., the area containing 50 % of the total scattering signal from an atom) are dominated by the broad tails and, therefore, will drastically overestimate the delocalisation of the central peak. Still, the currently usable range of energy losses falls roughly into the range between 300 eV (below which delocalisation becomes prohibitive) and around 1000 eV (above which the signal is too weak).

Similarly, one has to pick the 'best' high tension. In terms of spatial resolution, higher acceleration voltages are typically better due to the optical properties of the (scanning) transmission electron microscope. However, at the necessary small probes together with high required doses and long exposure times, extreme care must be taken not to damage the sample during the acquisition. So, generally, one can expect the best results at the highest acceleration voltage below the knock-on threshold of the investigated material.

Regarding data analysis, simulations are crucial to understand and correctly model the complex interplay between the probe beam and the sample.[59] While a directly interpretable image is generally the goal, of course, great care must be taken that under the chosen experimental conditions, the resulting maps indeed show what they seem to show, usually by corroborating with calculations. Luckily, the fundamental theory has already been developed to the point where it can describe the data very well within experimental accuracy. Improvements are always possible, such as going from an effective single-particle density functional theory model to a full many-body description, for example, based on the Bethe-Salpether equation, and including quasi-elastic effects (e.g., due to phonon scattering). Including many-particle effects such as the electron-hole interaction in the calculation would lead to improvements of the simulated near edge fine structure such as the correct ratio between the L_3 and L_2 intensities[60,61] and otherwise missing peaks due to excitonic effects.[62,63] However, it is not expected to affect the directional dependence, which is typically determined by the local environment (e.g., the direction to the nearest neighbouring atoms) and not by many-body effects. In addition, due to screening, the improvements are generally expected to be small[64–66] and the impact on the resulting maps of electronic transitions even smaller. For most experiments performed so far, the experimental difficulties effectively prevented visualising the fine details that might benefit most from more accurate models. For example, in order to directly compare experimental results and simulations, it is necessary to accurately reproduce shot noise as well as blurring due to partial coherence of the electron source[67] in the simulated maps. Effectively, thus far, the experimental challenges outweigh the theoretical ones.

This section lists many of the parameters that influence the mapping of orbital information. As stated at the beginning, this technique is right at the edge of what is currently possible even with the latest generation of transmission electron microscopes. This obviously implies that all the parameters need to be optimised for each individual experiment, and tough choices need to be made, typically between improving the spatial resolution and improving the SNR. Thus, no general, simple 'recipes' are currently available for mapping orbital information. However, previous studies showed that such mappings are possible.

Future improvements to both hardware and methodology will likely not only make mapping orbital information easier, but also broaden the range of materials it can be performed on.

5 | SUMMARY AND FUTURE PROSPECTS

Detecting and mapping electronic states at the atomic scale has been possible for a couple of decades with the advent of aberration correctors, and is now accessible to a large microscopy community with the widespread availability of stable aberration-corrected instruments and high-brightness electron guns. Chemical bonding of atomic species is reflected in the ELNES of core-level excitations. For instance, the chemical bonding anisotropy of oxygen atoms in the perovskite $SrTiO_3$, localised in octahedral sites with two Ti and four Sr nearest neighbour atoms, is reflected in the O-K near-edge structures. The anisotropic distribution of O $2p$ states was evidenced at the atomic scale after elastic and thermal diffuse scattering removal from the hyperspectral dataset,[70] while contrast variations in fine structure maps was studied more recently.[71]

The works highlighted in this review support the fact that one of the main challenges in mapping electronic orbitals is to relate the experimental contrast to the distribution of electronic orbitals. Considering the extremely weak signal that is sought after in mapping electronic transitions at atomic resolution, the experimental acquisition parameters must be thoroughly optimised.[56] Furthermore, robust data processing routines for noise minimisation and signal enhancement such as the removal of elastic and thermal diffuse scattering are of interest and provide an ingenious approach to recover a map of the inelastic scattering potential alone.[70,72,73] Additionally, full simulations of the fine structure maps appear necessary to interpret the experimental contrast. Simulated maps would combine the propagation of the electron beam using, for example, a multislice algorithm,[74] and the inelastic event from atomistic approaches using, for example, the mixed dynamic form factor.[38] The advent of direct electron detectors,[75–81] with much higher detective quantum efficiency compared to the conventional charge coupled device (CCD) and complementary metal-oxide semiconductor (CMOS), will surely help acquiring better quality data and exploring new systems, while optimising experimental parameters.

Additionally, the methodology itself could be improved. Possibilities range from the use of energy-filtered 4D STEM,[82–85] for example, to map specific electronic transitions using centre of mass reconstructions,[85] or ptychography[84,86–91] to obtain more information from a given experiment than just summing over the entire spectrometer entrance aperture to the use of beam shaping (e.g., a π-shaped beam[92,93] for probing transitions to p-states). All these methods come with their own sets of unique challenges, however. For example, using a non-circularly symmetric beam, one introduces yet another possible cause for directional dependence, and great care must be taken not to confuse this with a directional dependence caused by the sample. Nevertheless they are worth exploring and could potentially bring the next breakthrough for mapping orbital information.

Recent developments to detect other inelastic signals have emerged recently like secondary electron e-beam-induced current to image electronic densities or ionisation cross-sections of the electronic orbitals in encapsulated two-dimensional WSe_2.[94] Previously, probing core orbitals directly has been envisioned using energy dispersive X-ray spectroscopy, and has enabled evaluating the delocalisation of the core-state excitation.[95]

Finally, it should be emphasised that among accessible material systems, the strongest interest in electronic state distribution or orbital visualisation in the transmission electron microscope would be at interfaces and defects, which would help define and tune a wide range of material properties through so-called defect engineering. Recent studies have highlighted the potential and limitations of the STEM-EELS approach for such endeavour, for example, on crystals with reduced-dimension such as graphene.[40,41,68] In addition to the case of multilayer graphene that has been discussed above in Section 3.1, the prospect of mapping electronic states at point defect like substitutional N atoms or vacancies has been evaluated theoretically,[41] as illustrated in Figure 7A. The experimental detection of single-atom fine structure variations in graphene around, for example, vacancies,[96] N,[97] or Si dopants,[98,99] has now improved sufficiently from detector technology and acquisition strategies to enable electronic state mapping. As one of the most recent example, clear contrast variations in fine structure maps have been obtained in the recent work of Xu et al.,[68] which contributes to underline the potential of STEM-EELS for electronic state mapping at high spatial resolution (see Figure 7B–E). In the case of h-BN, the calculation of unoccupied π^* orbital maps at closed bilayer edges indicates strong intensity redistribution as compared to the pristine h-BN layer away from the edge,[69] as shown in Figure 7F and G. Although the calculations proved necessary to interpret EELS fine structure variations, it is likely that experimental orbital maps would enable a more accurate understanding of the electronic state redistribution at such three-dimensional defects. The range of systems of interest for which electronic state maps would provide relevant information goes well beyond 2D materials,
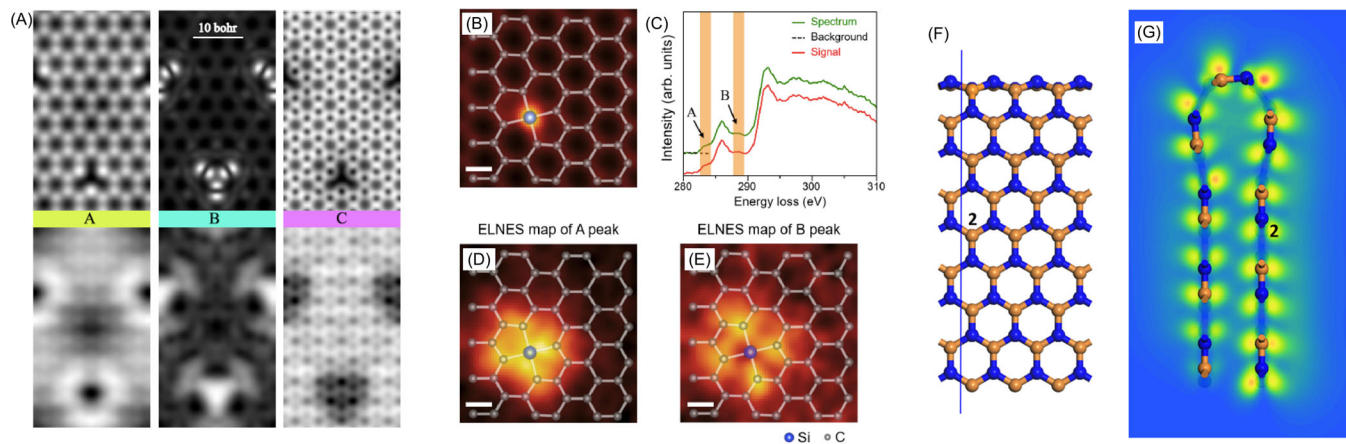
FIGURE 7 (A) Simulated TEM image of nitrogen-doped graphene. The three coloured areas indicate the energy ranges (A: 0–2 eV, B: 4–6 eV, and C: 8–10 eV) in the calculated local projected density of states (PDOS) (see fig. 1 in Pardini et al.[41] for details). 80 keV incident beam energy and lenses as in a probe-corrected instruments (upper panels) and a noncorrected microscope (bottom panels) were assumed. Reproduced with permission from Pardini et al.,[41] American Physical Society. (B–E) ELNES maps of the A and B peaks in the $Si - C_4$ configuration. (B) Representation of the simultaneously acquired STEM-ADF during EELS mapping, overlaid with the $Si - C_4$ atomic model. (C) A typical ELNES spectrum extracted from the 1st C atoms of the $Si - C_4$ defect configuration. Two orange regions label the energy windows of A and B peaks for the maps in (D) and (E), respectively. (D) The ELNES map of the A peak, overlaid with the $Si - C_4$ atomic model. (E) The ELNES map of the B peak, overlaid with the $Si - C_4$ atomic model. Scale bars: 0.2 nm. Reproduced with permission from Xu et al.,[68] American Physical Society. (F, G) Calculated orbital map at a closed bilayer edge in h-BN. (F) Depiction of the cross-sectional slice in bi-layer h-BN at which unoccupied orbitals have been plotted, and (G) EELS unoccupied orbital map, illustrating the unoccupied orbitals which have energy windows lying within the $\pi*$ region for the bulk-like position 2. Colours towards the red end of the spectrum indicate greater orbital intensity. Reproduced with permission from Alem et al.,[69] American Physical Society.

and includes crystalline hetero-interfaces where various quantum phenomena occur like charge concentration (e.g., two-dimensional electron gas at the $LaAlO_3$-TiO_2 interface[100]), and for which lattice strain could play a role. Other multidimensional systems where photon emission takes place, like quantum dots, could also benefit from electronic state mapping at atomic resolution. Should a defect luminesce, cathodoluminescence could provide substantial information on the optical properties of this defect. Recent advances in temporal coincidence measurements between EELS and cathodoluminescence, driven by the development of time-resolved direct electron detectors, in STEM instruments equipped with a standard field emission electron gun could also help determining the excitation channel and the decay pathway at the origin of a specific photon emission,[80] whereas polarised electron beams could unveil symmetry-constrained phenomena.[92] In spite of a spatial resolution limited to a few nm[101,102] and the relative lack of aberration-corrected STEM instruments equipped with a cathodoluminescence mirror, cathodoluminescence appears as a complementary tool to the broadband absorption EEL spectroscopy.

This review was motivated by the recent methodological and technological developments in transmission electron microscopy that enabled atomic-resolution analysis of the electronic structure of solids, towards so-called electronic

orbital mapping. Although proof-of-principle experiments have been reported, much work remains to be achieved to enable electronic state mapping in a robust, reproducible and interpretable fashion at specific and relevant areas of solids, like crystal discontinuities. The current state of the art in this field shows that inelastic scattering in real space bears a strong potential using, for example, STEM-EELS, but inelastic scattering in reciprocal space is also of huge interest via, for example, energy-filtered diffraction signals coupled to the high sampling and spatial-resolution capabilities of 4D-STEM. The advantages and disadvantages of these approaches, in addition to the inherent challenges of electronic state mapping at atomic resolution and its interpretation in terms of site- and momentum-projected orbitals, are discussed in this work. Beyond the information carried by incident electrons and their energy lost during inelastic scattering, novel approaches that rely on seldom used signals, like secondary electron ebeam-induced current, appear promising. The proposed approaches to map electronic states at high spatial resolution could be complemented with the plethora of signals now accessible within the aberration-corrected transmission electron microscope, such as phonons through vibrational EELS[103,104] and photons emitted from point defects through cathodoluminescence,[105] to refine even further the nature of atomic bonding and the properties

of individual defects. Spatially resolved vibrational excitations using EELS, which have been evidenced down to atomic resolution,[106,107] at defects and interfaces[108–113] and single atoms,[114,115] could enable access to electron-phonon interactions[116] and to the directionality of phonon modes. Specifically, the vibrational anisotropy of oxygen atoms in $SrTiO_3$, recently measured by momentum-selective dark-field vibrational EELS,[117] suggests that the directionality of phonon modes mapped at atomic resolution may contain information about the directionality of bonding between atoms, which relates to electronic orbitals. Therefore, vibrational EELS may provide additional information about the projected symmetry and spatial extent of electronic states in favourable cases. Fundamental quantum limits of signal detection and precision of measurements are currently being investigated, such as the recent theoretical evaluation of the quantum limits for the position of single atoms from elastic scattering as a function of electron dose.[118] In the context of mapping electronic state and orbitals, concepts of an inherently quantum nature, the quantum limit for inelastic scattered signals at, for example, crystal discontinuities would be important to explore in the future. The authors hope that this review will stimulate the interest of a wide range of scientists and inspire new contributors to further advancing the analytical capabilities of the transmission electron microscope.

ACKNOWLEDGEMENTS

CONFLICT OF INTEREST STATEMENT

The authors declare that they have no conflict of interest.

ORCID

M. Bugnet 🔵 https://orcid.org/0000-0002-8272-8964
S. Löffler 🔵 https://orcid.org/0000-0003-0080-2495
M. Ederer 🔵 https://orcid.org/0000-0002-8441-9778
D. M. Kepaptsoglou 🔵 https://orcid.org/0000-0003-0499-0470
Q. M. Ramasse 🔵 https://orcid.org/0000-0001-7466-2283

REFERENCES

1. Vogt, C., & Weckhuysen, B. M. (2022). The concept of active site in heterogeneous catalysis. *Nature Reviews Chemistry*, 6(2), 89–111. https://doi.org/10.1038/s41570-021-00340-y
2. Zhang, Z., & Lagally, M. G. (1997). Atomistic processes in the early stages of thin-film growth. *Science*, 276(5311), 377–383. https://doi.org/10.1126/science.276.5311.377
3. Pantelides, S. T. (1978). The electronic structure of impurities and other point defects in semiconductors. *Reviews of Modern Physics*, 50(4), 797. https://doi.org/10.1103/RevModPhys.50.797
4. Moore, E. A., & Smart, L. E. (Eds.) (2020). *Optical properties of solids*. In Solid state chemistry (pp. 283–314). CRC Press. https://doi.org/10.1201/9780429027284-8
5. Lherbier, A., Dubois, S. M. M., Declerck, X., Niquet, Y. M., Roche, S., & Charlier, J. C. (2012). Transport properties of graphene containing structural defects. *Physical Review B*, 86(7), 075402. https://doi.org/10.1103/PhysRevB.86.075402
6. Hirth, J. P. (1972). The influence of grain boundaries on mechanical properties. *Metallurgical Transactions*, 3, 3047–3067. https://doi.org/10.1007/BF02661312
7. Yavaş, H., Sundermann, M., Chen, K., Amorese, A., Severing, A., Gretarsson, H., Haverkort, M. W., & Tjeng, L. H. (2019). Direct imaging of orbitals in quantum materials. *Nature Physics*, 15(6), 559–562. https://doi.org/10.1038/s41567-019-0471-2
8. Hafiz, H., Suzuki, K., Barbiellini, B., Orikasa, Y., Callewaert, V., Kaprzyk, S., Itou, M., Yamamoto, K., Yamada, R., Uchimoto, Y., Sakurai, Y., Sakurai, H., & Bansil, A. (2017). Visualizing redox orbitals and their potentials in advanced lithium-ion battery materials using high-resolution x-ray Compton scattering. *Science Advances*, 3(8), e1700971. https://doi.org/10.1126/sciadv.1700971
9. Zuo, J. M., Kim, M., O'keeffe, M., & Spence, J. C. H. (1999). Direct observation of d-orbital holes and Cu-Cu bonding in Cu_2O. *Nature (London)*, 401(6748), 49–52. https://doi.org/10.1038/43403
10. Nakashima, P. N. H., Smith, A. E., Etheridge, J., & Muddle, B. C. (2011). The bonding electron density in aluminum. *Science*, 331(6024), 1583–1586. https://doi.org/10.1126/science.1198543
11. Meyer, J. C., Kurasch, S., Park, H. J., Skakalova, V., Künzel, D., Groß, A., Chuvilin, A., Algara-Siller, G., Roth, S., Iwasaki, T., Starke, U., Smet, J. H., & Kaiser, U. (2011). Experimental analysis of charge redistribution due to chemical bonding by high-resolution transmission electron microscopy. *Nature Materials*, 10(3), 209–215. https://doi.org/10.1038/nmat2941
12. Müller, K., Krause, F. F., Béché, A., Schowalter, M., Galioit, V., Löffler, S., Verbeeck, J., Zweck, J., Schattschneider, P., & Rosenauer, A. (2014). Atomic electric fields revealed by a quantum mechanical approach to electron picodiffraction. *Nature Communications*, 5(1), 1–8. https://doi.org/10.1038/ncomms6653
13. Gao, W., Addiego, C., Wang, H., Yan, X., Hou, Y., Ji, D., Heikes, C., Zhang, Y., Li, L., Huyan, H., Blum, T., Aoki, T., Nie, Y., Schlom, D. G., Wu, R., & Pan, X. (2019). Real-space charge-density imaging with sub-Ångström resolution by four-dimensional electron microscopy. *Nature (London)*, 575(7783), 480–484. https://doi.org/10.1038/s41586-019-1649-6
14. Sánchez-Santolino, G., Lugg, N. R., Seki, T., Ishikawa, R., Findlay, S. D., Kohno, Y., Kanitani, Y., Tanaka, S., Tomiya, S., Ikuhara, Y., & Shibata, N. (2018). Probing the internal atomic

charge density distributions in real space. *ACS Nano*, *12*(9), 8875–8881. https://doi.org/10.1021/acsnano.8b03712

15. Addiego, C., Gao, W., Huyan, H., & Pan, X. (2023). Probing charge density in materials with atomic resolution in real space. *Nature Reviews Physics*, *5*, 117–132. https://doi.org/10.1038/s42254-022-00541-4

16. Schwarz, W. H. E. (2006). Measuring orbitals: Provocation or reality? *Angewandte Chemie International Edition*, *45*(10), 1508–1517. https://doi.org/10.1002/anie.200501333

17. Itatani, J., Zeidler, D., Levesque, J., Spanner, M., Villeneuve, D. M., & Corkum, P. B. (2005). Controlling high harmonic generation with molecular wave packets. *Physical Review Letters*, *94*, 123902. https://doi.org/10.1103/PhysRevLett.94.123902

18. Itatani, J., Levesque, J., Zeidler, D., Niikura, H., Pépin, H., Kieffer, J. C., Corkum, P. B., & Villeneuve, D. M. (2004). Tomographic imaging of molecular orbitals. *Nature (London)*, *432*, 867–871. https://doi.org/10.1038/nature03183

19. Brion, C. E., Cooper, G., Zheng, Y., Litvinyuk, I. V., & McCarthy, I. E. (2001). Imaging of orbital electron densities by electron momentum spectroscopy – A chemical interpretation of the binary (e,2e) reaction. *Chemical Physics*, *270*(1), 13–30. https://doi.org/10.1016/S0301-0104(01)00385-8

20. Puschnig, P., Berkebile, S., Fleming, A. J., Koller, G., Emtsev, K., Seyller, T., Riley, J. D., Ambrosch-Draxl, C., Netzer, F. P., & Ramsey, M. G. (2009). Reconstruction of molecular orbital densities from photoemission data. *Science*, *326*(5953), 702–706. https://doi.org/10.1126/science.1176105

21. Repp, J., Meyer, G., Paavilainen, S., Olsson, F. E., & Persson, M. (2006). Imaging bond formation between a gold atom and pentacene on an insulating surface. *Science*, *312*(5777), 1196–1199. https://doi.org/10.1126/science.1126073

22. Repp, J., Meyer, G., Stojković, S. M., Gourdon, A., & Joachim, C. (2005). Molecules on insulating films: Scanning-tunneling microscopy imaging of individual molecular orbitals. *Physical Review Letters*, *94*(2), 026803. https://doi.org/10.1103/PhysRevLett.94.026803

23. Gross, L., Moll, N., Mohn, F., Curioni, A., Meyer, G., Hanke, F., & Persson, M. (2011). High-resolution molecular orbital imaging using a p-wave STM tip. *Physical Review Letters*, *107*(8), 086101. https://doi.org/10.1103/PhysRevLett.107.086101

24. Egerton, R. F. (2011). Electron energy-loss spectroscopy in the electron microscope. Springer Science & Business Media. https://doi.org/10.1007/978-1-4419-9583-4

25. Radtke, G., & Botton, G. A. (2011). Energy loss near-edge structures. In: S.J. Pennycook & P.D. Nellist (Eds.), *Scanning transmission electron microscopy imaging and analysis* (pp. 207–245). New York: Springer Science Business Media. https://doi.org/10.1007/978-1-4419-7200-2_5

26. Bosman, M., Keast, V. J., Garcia-Munoz, J. L., D'Alfonso, A. J., Findlay, S. D., & Allen, L. J. (2007). Two-dimensional mapping of chemical information at atomic resolution. *Physical Review Letters*, *99*(8), 086102. https://doi.org/10.1103/PhysRevLett.99.086102

27. Kimoto, K., Asaka, T., Nagai, T., Saito, M., Matsui, Y., & Ishizuka, K. (2007). Element-selective imaging of atomic columns in a crystal using stem and eels. *Nature (London)*, *450*(7170), 702–704. https://doi.org/10.1038/nature06352

28. Muller, D. A., Kourkoutis, L. F., Murfitt, M., Song, J. H., Hwang, H. Y., Silcox, J., Dellby, N., & Krivanek, O. L. (2008). Atomic-scale chemical imaging of composition and bonding by aberration-corrected microscopy. *Science*, *319*(5866), 1073–1076. https://doi.org/10.1126/science.1148820

29. Varela, M., Oxley, M. P., Luo, W., Tao, J., Watanabe, M., Lupini, A. R., Pantelides, S. T., & Pennycook, S. J. (2009). Atomic-resolution imaging of oxidation states in manganites. *Physical Review B*, *79*(8), 085117. https://doi.org/10.1103/PhysRevB.79.085117

30. Tan, H., Turner, S., Yücelen, E., Verbeeck, J., & Van Tendeloo, G. (2011). 2D atomic mapping of oxidation states in transition metal oxides by scanning transmission electron microscopy and electron energy-loss spectroscopy. *Physical Review Letters*, *107*(10), 107602. https://doi.org/10.1103/PhysRevLett.107.107602

31. Klie, R. F., Qiao, Q., Paulauskas, T., Gulec, A., Rebola, A., Öğüt, S., Prange, M. P., Idrobo, J. C., Pantelides, S. T., Kolesnik, S., Dabrowski, B., Ozdemir, M., Boyraz, C., Mazumdar, D., & Gupta, A. (2012). Observations of Co^{4+} in a higher spin state and the increase in the seebeck coefficient of thermoelectric $Ca_3Co_4O_9$. *Physical Review Letters*, *108*(19), 196601. https://doi.org/10.1103/PhysRevLett.108.196601

32. Gauquelin, N., Benckiser, E., Kinyanjui, M. K., Wu, M., Lu, Y., Christiani, G., Logvenov, G., Habermeier, H. U., Kaiser, U., Keimer, B., & Botton, G. A. (2014). Atomically resolved eels mapping of the interfacial structure of epitaxially strained LaNiO3/LaAlO3 superlattices. *Physical Review B*, *90*(19), 195140. https://doi.org/10.1103/PhysRevB.90.195140

33. Bugnet, M., Löffler, S., Hawthorn, D., Dabkowska, H. A., Luke, G. M., Schattschneider, P., Sawatzky, G. A., Radtke, G., & Botton, G. A. (2016). Real-space localization and quantification of hole distribution in chain-ladder $Sr_3Ca_{11}Cu_{24}O_{41}$ superconductor. *Science Advances*, *2*(3), e1501652. https://doi.org/10.1126/sciadv.1501652

34. Gloter, A., Badjeck, V., Bocher, L., Brun, N., March, K., Marinova, M., Tencé, M., Walls, M., Zobelli, A., Stéphan, O., & Colliex, C. (2017). Atomically resolved mapping of eels fine structures. *Materials Science in Semiconductor Processing*, *65*, 2–17. doi: https://doi.org/10.1016/j.mssp.2016.07.006

35. Haruta, M., Fujiyoshi, Y., Nemoto, T., Ishizuka, A., Ishizuka, K., & Kurata, H. (2018). Atomic-resolution two-dimensional mapping of holes in the cuprate superconductor $La_{2-x}Sr_xCuO_{4\pm\delta}$. *Physical Review B*, *97*(20), 205139. https://doi.org/10.1103/PhysRevB.97.205139

36. Wang, Y., Huang, M. R. S., Salzberger, U., Hahn, K., Sigle, W., & van Aken, P. A. (2018). Towards atomically resolved eels elemental and fine structure mapping via multi-frame and energy-offset correction spectroscopy. *Ultramicroscopy*, *184*, 98–105. https://doi.org/10.1016/j.ultramic.2017.10.014

37. Radtke, G., Hennes, M., Bugnet, M., Ramasse, Q. M., Weng, X., Demaille, D., Gobaut, B., Ohresser, P., Otero, E., Choueikani, F., Juhin, A., Sainctavit, P., Zheng, Y., & Vidal, F. (2019). Atomic-scale study of metal-oxide interfaces and magnetoelastic coupling in self-assembled epitaxial vertically aligned magnetic nanocomposites. *Advanced Materials Interfaces*, *6*(17), 1900549. https://doi.org/10.1002/admi.201900549

38. Löffler, S., Motsch, V., & Schattschneider, P. (2013). A pure state decomposition approach of the mixed dynamic form factor for mapping atomic orbitals. *Ultramicroscopy*, *131*, 39–45. https://doi.org/10.1016/j.ultramic.2013.03.021

39. Löffler, S., Bugnet, M., Gauquelin, N., Lazar, S., Assmann, E., Held, K., Botton, G. A., & Schattschneider, P. (2017). Real-space mapping of electronic orbitals. *Ultramicroscopy*, *177*, 26–29. https://doi.org/10.1016/j.ultramic.2017.01.018

40. Bugnet, M., Ederer, M., Lazarov, V. K., Li, L., Ramasse, Q. M., Löffler, S., & Kepaptsoglou, D. M. (2022). Imaging the spatial distribution of electronic states in graphene using electron energy-loss spectroscopy: Prospect of orbital mapping. *Physical Review Letters*, *128*, 116401. https://doi.org/10.1103/PhysRevLett.128.116401

41. Pardini, L., Löffler, S., Biddau, G., Hambach, R., Kaiser, U., Draxl, C., & Schattschneider, P. (2016). Mapping atomic orbitals with the transmission electron microscope: Images of defective graphene predicted from first-principles theory. *Physical Review Letters*, *117*, 036801. https://doi.org/10.1103/PhysRevLett.117.036801

42. Forbes, B. D., Houben, L., Mayer, J., Dunin-Borkowski, R. E., & Allen, L. J. (2014). Elemental mapping in achromatic atomic-resolution energy-filtered transmission electron microscopy. *Ultramicroscopy*, *147*, 98–105. https://doi.org/10.1016/j.ultramic.2014.07.002

43. Urban, K. W., Mayer, J., Jinschek, J. R., Neish, M. J., Lugg, N. R., & Allen, L. J. (2013). Achromatic elemental mapping beyond the nanoscale in the transmission electron microscope. *Physical Review Letters*, *110*(18), 185507. https://doi.org/10.1103/PhysRevLett.110.185507

44. Mohn, M. J., Biskupek, J., Lee, Z., Rose, H., & Kaiser, U. (2020). Lattice contrast in the core-loss EFTEM signal of graphene. *Ultramicroscopy*, *219*, 113119. https://doi.org/10.1016/j.ultramic.2020.113119

45. Krivanek, O. L., Kundmann, M. K., & Kimoto, K. (1995). Spatial resolution in EFTEM elemental maps. *Journal of Microscopy*, *180*(3), 277–287. https://doi.org/10.1111/j.1365-2818.1995.tb03686.x

46. Löffler, S., Ennen, I., Tian, F., Schattschneider, P., & Jaouen, N. (2011). Breakdown of the dipole approximation in core losses. *Ultramicroscopy*, *111*(8), 1163–1167. https://doi.org/10.1016/j.ultramic.2011.03.006

47. Botton, G. A. (2005). A new approach to study bonding anisotropy with eels. *Journal of Electron Spectroscopy and Related Phenomena*, *143*(2–3), 129–137. https://doi.org/10.1016/j.elspec.2004.09.023

48. Fossard, F., Sponza, L., Schué, L., Attaccalite, C., Ducastelle, F., Barjon, J., & Loiseau, A. (2017). Angle-resolved electron energy loss spectroscopy in hexagonal boron nitride. *Physical Review B*, *96*(11), 115304. https://doi.org/10.1103/physrevb.96.115304

49. Leapman, R. D., Fejes, P. L., & Silcox, J. (1983). Orientation dependence of core edges from anisotropic materials determined by inelastic scattering of fast electrons. *Physical Review B*, *28*(5), 2361. https://doi.org/10.1103/PhysRevB.28.2361

50. Hébert, C., Schattschneider, P., Franco, H., & Jouffrey, B. (2006). ELNES at magic angle conditions. *Ultramicroscopy*, *106*(11–12), 1139–1143. https://doi.org/10.1016/j.ultramic.2006.04.030

51. Sato, Y., Bugnet, M., Terauchi, M., Botton, G. A., & Yoshiasa, A. (2016). Heterogeneous diamond phases in compressed graphite studied by electron energy-loss spectroscopy. *Diamond and Related Materials*, *64*, 190–196. https://doi.org/10.1016/j.diamond.2016.02.010

52. Freeman, H. M., Jones, A. N., Ward, M. B., Hage, F. S., Tzelepi, N., Ramasse, Q. M., Scott, A. J., & Brydson, R. M. D. (2016). On the nature of cracks and voids in nuclear graphite. *Carbon*, *103*, 45–55. https://doi.org/10.1016/j.carbon.2016.03.011

53. Taftø, J., & Krivanek, O. L. (1982). Site-specific valence determination by electron energy-loss spectroscopy. *Physical Review Letters*, *48*(8), 560–563. https://doi.org/10.1103/PhysRevLett.48.560

54. Tatsumi, K., & Muto, S. (2009). Local electronic structure analysis by site-selective ELNES using electron channeling and first-principles calculations. *Journal of Physics: Condensed Matter*, *21*(10), 104213. https://doi.org/10.1088/0953-8984/21/10/104213

55. Hetaba, W., Löffler, S., Willinger, M. G., Schuster, M. E., Schlögl, R., & Schattschneider, P. (2014). Site-specific ionisation edge fine-structure of rutile in the electron microscope. *Micron*, *63*, 15–19. https://doi.org/10.1016/j.micron.2014.02.008

56. Ederer, M., & Löffler, S. (2024). Optimizing experimental parameters for orbital mapping. *Ultramicroscopy*, *256*, 113866. https://doi.org/10.1016/j.ultramic.2023.113866

57. Egerton, R. F. (2009). Electron energy-loss spectroscopy in the TEM. *Reports on Progress in Physics*, *72*(1), 016502. https://doi.org/10.1088/0034-4885/72/1/016502

58. Schattschneider, P., Nelhiebel, M., & Jouffrey, B. (1999). Density matrix of inelastically scattered fast electrons. *Physical Review B*, *59*(16), 10959–10969. https://doi.org/10.1103/PhysRevB.59.10959

59. Iwashimizu, C., Haruta, M., Nemoto, T., & Kurata, H. (2023). Different atomic contrasts in HAADF images and EELS maps of rutile TiO_2. *Microscopy*, *72*(4), 353–360. https://doi.org/10.1093/jmicro/dfac067

60. Shirley, E. L. (2005). Bethe-Salpeter treatment of x-ray absorption including core-hole multiplet effects. *Journal of Electron Spectroscopy and Related Phenomena*, *144–147*, 1187–1190. https://doi.org/10.1016/j.elspec.2005.01.191

61. Laskowski, R., & Blaha, P. (2010). Understanding the $L_{2,3}$ x-ray absorption spectra of early 3*d* transition elements. *Physical Review B*, *82*, 205104. https://doi.org/10.1103/PhysRevB.82.205104

62. Albrecht, S., Reining, L., Del Sole, R., & Onida, G. (1998). Ab initio calculation of excitonic effects in the optical spectra of semiconductors. *Physical Review Letters*, *80*, 4510–4513. https://doi.org/10.1103/PhysRevLett.80.4510

63. Benedict, L. X., Shirley, E. L., & Bohn, R. B. (1998). Optical absorption of insulators and the electron-hole interaction: An ab initio calculation. *Physical Review Letters*, *80*, 4514–4517. https://doi.org/10.1103/PhysRevLett.80.4514

64. Rohlfing, M., & Louie, S. G. (1998). Electron-hole excitations in semiconductors and insulators. *Physical Review Letters*, *81*, 2312–2315. https://doi.org/10.1103/PhysRevLett.81.2312

65. Arnaud, B., & Alouani, M. (2001). Local-field and excitonic effects in the calculated optical properties of semiconductors from first-principles. *Physical Review B*, *63*, 085208. https://doi.org/10.1103/PhysRevB.63.085208

66. Puschnig, P., & Ambrosch-Draxl, C. (2002). Optical absorption spectra of semiconductors and insulators including electron-hole correlations: An ab initio study within the LAPW method.

Physical Review B, *66*, 165105. https://doi.org/10.1103/PhysRevB.66.165105

67. Schattschneider, P., Stöger-Pollach, M., Löffler, S., Steiger-Thirsfeld, A., Hell, J., & Verbeeck, J. (2012). Sub-nanometer free electrons with topological charge. *Ultramicroscopy*, *115*, 21–25. https://doi.org/10.1016/j.ultramic.2012.01.010

68. Xu, M., Li, A., Pennycook, S. J., Gao, S. P., & Zhou, W. (2023). Probing a defect-site-specific electronic orbital in graphene with single-atom sensitivity. *Physical Review Letters*, *131*, 186202. https://doi.org/10.1103/PhysRevLett.131.186202

69. Alem, N., Ramasse, Q. M., Seabourne, C. R., Yazyev, O. V., Erickson, K., Sarahan, M. C., Kisielowski, C., Scott, A. J., Louie, S. G., & Zettl, A. (2012). Subangstrom edge relaxations probed by electron microscopy in hexagonal boron nitride. *Physical Review Letters*, *109*, 205502. https://doi.org/10.1103/PhysRevLett.109.205502

70. Neish, M. J., Lugg, N. R., Findlay, S. D., Haruta, M., Kimoto, K., & Allen, L. J. (2013). Detecting the direction of oxygen bonding in $SrTiO_3$. *Physical Review B*, *88*(11), 115120. https://doi.org/10.1103/PhysRevB.88.115120

71. Iwashimizu, C., Haruta, M., & Kurata, H. (2021). Electron orbital mapping of $SrTiO_3$ using electron energy-loss spectroscopy. *Applied Physics Letters*, *119*(23), 232902. https://doi.org/10.1063/5.0072190

72. Lugg, N. R., Haruta, M., Neish, M. J., Findlay, S. D., Mizoguchi, T., Kimoto, K., & Allen, L. J. (2012). Removing the effects of elastic and thermal scattering from electron energy-loss spectroscopic data. *Applied Physics Letters*, *101*(18), 183112. https://doi.org/10.1063/1.4765657

73. Lugg, N. R., Neish, M. J., Findlay, S. D., & Allen, L. J. (2014). Practical aspects of removing the effects of elastic and thermal diffuse scattering from spectroscopic data for single crystals. *Microscopy and Microanalysis*, *20*(4), 1078–1089. https://doi.org/10.1017/S1431927614000804

74. Kirkland, E. J. (1998). Advanced computing in electron microscopy. Plenum Press. https://doi.org/10.1007/978-3-030-33260-0

75. Hart, J. L., Lang, A. C., Leff, A. C., Longo, P., Trevor, C., Twesten, R. D., & Taheri, M. L. (2017). Direct detection electron energy-loss spectroscopy: A method to push the limits of resolution and sensitivity. *Scientific Reports*, *7*(1), 8243. doi: https://doi.org/10.1038/s41598-017-07709-4

76. Mir, J. A., Clough, R., MacInnes, R., Gough, C., Plackett, R., Shipsey, I., Sawada, H., MacLaren, I., Ballabriga, R., Maneuski, D., O'Shea, V., McGrouther, D., & Kirkland, A. I. (2017). Characterisation of the Medipix3 detector for 60 and 80 keV electrons. *Ultramicroscopy*, *182*, 44–53. https://doi.org/10.1016/j.ultramic.2017.06.010

77. Ruiz Caridad, A., Erni, R., Vogel, A., & Rossell, M. D. (2022). Applications of a novel electron energy filter combined with a hybrid-pixel direct electron detector for the analysis of functional oxides by STEM/EELS and energy-filtered imaging. *Micron*, *160*, 103331. https://doi.org/10.1016/j.micron.2022.103331

78. Cheng, S., Pofelski, A., Longo, P., Twesten, R. D., Zhu, Y., & Botton, G. A. (2020). The performance evaluation of direct detection electron energy-loss spectroscopy at 200 kv and 80 kv accelerating voltages. *Ultramicroscopy*, *212*, 112942. https://doi.org/10.1016/j.ultramic.2020.112942

79. Plotkin-Swing, B., Corbin, G. J., De Carlo, S., Dellby, N., Hoermann, C., Hoffman, M. V., Lovejoy, T. C., Meyer, C. E., Mittelberger, A., Pantelic, R., Piazza, L., & Krivanek, O. L. (2020). Hybrid pixel direct detector for electron energy loss spectroscopy. *Ultramicroscopy*, *217*, 113067. https://doi.org/10.1016/j.ultramic.2020.113067

80. Varkentina, N., Auad, Y., Woo, S. Y., Zobelli, A., Bocher, L., Blazit, J. D., Li, X., Tencé, M., Watanabe, K., Taniguchi, T., Stéphan, O., Kociak, M., & Tizei, L. H. G. (2022). Cathodoluminescence excitation spectroscopy: Nanoscale imaging of excitation pathways. *Science Advances*, *8*(40), eabq4947. https://doi.org/10.1126/sciadv.abq4947

81. Auad, Y., Walls, M., Blazit, J. D., Stéphan, O., Tizei, L. H. G., Kociak, M., De la Peña, F., & Tencé, M. (2022). Event-based hyperspectral EELS: Towards nanosecond temporal resolution. *Ultramicroscopy*, *239*, 113539. https://doi.org/10.1016/j.ultramic.2022.113539

82. Müller-Caspary, K., Krause, F. F., Grieb, T., Löffler, S., Schowalter, M., Béché, A., Galioit, V., Marquardt, D., Zweck, J., Schattschneider, P., Verbeeck, J., & Rosenauer, A. (2017). Measurement of atomic electric fields and charge densities from average momentum transfers using scanning transmission electron microscopy. *Ultramicroscopy*, *178*, 62–80. https://doi.org/10.1016/j.ultramic.2016.05.004

83. Löffler, S., & Ederer, M. (2023). 4D energy-filtered stem: A new approach for mapping orbital transitions. *Microscopy and Microanalysis*, *29*(S1), 376. https://doi.org/10.1093/micmic/ozad067.176

84. Ophus, C. (2019). Four-dimensional scanning transmission electron microscopy (4D-STEM): From scanning nanodiffraction to ptychography and beyond. *Microscopy and Microanalysis*, *25*(3), 563–582. https://doi.org/10.1017/S1431927619000497

85. Haas, B., & Koch, C. T. (2022). Momentum-and energy-resolved stem at atomic resolution. *Microscopy and Microanalysis*, *28*(S1), 406–408. https://doi.org/10.1017/S1431927622002343

86. Rodenburg, J. M. (2008). Ptychography and related diffractive imaging methods. *Advances in Imaging and Electron Physics*, *150*, 87–184. https://doi.org/10.1016/S1076-5670(07)00003-1

87. Yang, H., Rutte, R. N., Jones, L., Simson, M., Sagawa, R., Ryll, H., Huth, M., Pennycook, T. J., Green, M. L. H., Soltau, H., Kondo, Y., Davis, B. G., & Nellist, P. D. (2016). Simultaneous atomic-resolution electron ptychography and z-contrast imaging of light and heavy elements in complex nanostructures. *Nature Communications*, *7*(1), 12532. https://doi.org/10.1038/ncomms12532

88. Pennycook, T. J., Lupini, A. R., Yang, H., Murfitt, M. F., Jones, L., & Nellist, P. D. (2015). Efficient phase contrast imaging in stem using a pixelated detector. Part 1: Experimental demonstration at atomic resolution. *Ultramicroscopy*, *151*, 160–167. https://doi.org/10.1016/j.ultramic.2014.09.013

89. Song, J., Allen, C. S., Gao, S., Huang, C., Sawada, H., Pan, X., Warner, J., Wang, P., & Kirkland, A. I. (2019). Atomic resolution defocused electron ptychography at low dose with a fast, direct electron detector. *Scientific Reports*, *9*(1), 3919. https://doi.org/10.1038/s41598-019-40413-z

90. Jiang, Y., Chen, Z., Han, Y., Deb, P., Gao, H., Xie, S., Purohit, P., Tate, M. W., Park, J., Gruner, S. M., Elser, V., & Muller, D. A. (2018). Electron ptychography of 2D materials to deep

sub-Ångström resolution. *Nature (London)*, *559*(7714), 343–349. https://doi.org/10.1038/s41586-018-0298-5

91. Martinez, G. T., Shi, B. X., Naginey, T. C., Jones, L., O'Leary, C. M., Pennycook, T. J., Nicholls, R. J., Yates, J. R., & Nellist, P. D. (2019). Direct imaging of charge redistribution due to bonding at atomic resolution via electron ptychography. *arXiv preprint arXiv:1907.12974*. https://doi.org/10.48550/arXiv.1907.12974

92. Guzzinati, G., Béché, A., Lourenço-Martins, H., Martin, J., Kociak, M., & Verbeeck, J. (2017). Probing the symmetry of the potential of localized surface plasmon resonances with phase-shaped electron beams. *Nature Communications*, *8*, 14999. https://doi.org/10.1038/ncomms14999

93. Lourenço-Martins, H., Lubk, A., & Kociak, M. (2021). Bridging nano-optics and condensed matter formalisms in a unified description of inelastic scattering of relativistic electron beams. *SciPost Physics*, *10*(2), 031. https://doi.org/10.21468/SciPostPhys.10.2.031

94. Dyck, O., Almutlaq, J., Lingerfelt, D., Swett, J. L., Oxley, M. P., Huang, B., Lupini, A. R., Englund, D., & Jesse, S. (2023). Direct imaging of electron density with a scanning transmission electron microscope. *Nature Communications*, *14*(1), 7550. https://doi.org/10.1038/s41467-023-42256-9

95. Jeong, J. S., Odlyzko, M. L., Xu, P., Jalan, B., & Mkhoyan, K. A. (2016). Probing core-electron orbitals by scanning transmission electron microscopy and measuring the delocalization of core-level excitations. *Physical Review B*, *93*(16), 165140. https://doi.org/10.1103/physrevb.93.165140

96. Suenaga, K., & Koshino, M. (2010). Atom-by-atom spectroscopy at graphene edge. *Nature (London)*, *468*(7327), 1088–1090. https://doi.org/10.1038/nature09664

97. Kepaptsoglou, D. M., Hardcastle, T. P., Seabourne, C. R., Bangert, U., Zan, R., Amani, J. A., Hofsäss, H., Nicholls, R. J., Brydson, R. M. D., Scott, A. J., & Ramasse, Q. M. (2015). Electronic structure modification of ion implanted graphene: The spectroscopic signatures of p-and n-type doping. *ACS Nano*, *9*(11), 11398–11407. https://doi.org/10.1021/acsnano.5b05305

98. Ramasse, Q. M., Seabourne, C. R., Kepaptsoglou, D. M., Zan, R., Bangert, U., & Scott, A. J. (2013). Probing the bonding and electronic structure of single atom dopants in graphene with electron energy loss spectroscopy. *Nano Letters*, *13*(10), 4989–4995. https://doi.org/10.1021/nl304187e

99. Zhou, W., Kapetanakis, M. D., Prange, M. P., Pantelides, S. T., Pennycook, S. J., & Idrobo, J. C. (2012). Direct determination of the chemical bonding of individual impurities in graphene. *Physical Review Letters*, *109*(20), 206803. https://doi.org/10.1103/PhysRevLett.109.206803

100. Oberaigner, M., Ederer, M., Chaluvadi, S. K., Orgiani, P., Ciancio, R., Löffler, S., Kothleitner, G., & Knez, D. (2023). Visualising emergent phenomena at oxide interfaces. *arXiv preprint arXiv:2310.03863*. https://doi.org/10.48550/arXiv.2310.03863

101. Coenen, T., & Haegel, N. M. (2017). Cathodoluminescence for the 21st century: Learning more from light. *Applied Physics Reviews*, *4*(3), 031103. https://doi.org/10.1063/1.4985767

102. Kociak, M., & Zagonel, L. F. (2017). Cathodoluminescence in the scanning transmission electron microscope. *Ultramicroscopy*, *176*, 112–131. https://doi.org/10.1016/j.ultramic.2017.03.014

103. Krivanek, O. L., Lovejoy, T. C., Dellby, N., Aoki, T., Carpenter, R. W., Rez, P., Soignard, E., Zhu, J., Batson, P. E., Lagos, M. J., Egerton, R. F., & Crozier, P. A. (2014). Vibrational spectroscopy in the electron microscope. *Nature (London)*, *514*(7521), 209–212. https://doi.org/10.1038/nature13870

104. Miyata, T., Fukuyama, M., Hibara, A., Okunishi, E., Mukai, M., & Mizoguchi, T. (2014). Measurement of vibrational spectrum of liquid using monochromated scanning transmission electron microscopy–electron energy loss spectroscopy. *Journal of Electron Microscopy*, *63*(5), 377–382. https://doi.org/10.1093/jmicro/dfu023

105. Bourrellier, R., Meuret, S., Tararan, A., Stéphan, O., Kociak, M., Tizei, L. H. G., & Zobelli, A. (2016). Bright UV single photon emission at point defects in h-BN. *Nano Letters*, *16*(7), 4317–4321. https://doi.org/10.1021/acs.nanolett.6b01368

106. Hage, F. S., Kepaptsoglou, D. M., Ramasse, Q. M., & Allen, L. J. (2019). Phonon spectroscopy at atomic resolution. *Physical Review Letters*, *122*(1), 016103. https://doi.org/10.1103/PhysRevLett.122.016103

107. Venkatraman, K., Levin, B. D. A., March, K., Rez, P., & Crozier, P. A. (2019). Vibrational spectroscopy at atomic resolution with electron impact scattering. *Nature Physics*, *15*(12), 1237–1241. https://doi.org/10.1038/s41567-019-0675-5

108. Yan, X., Liu, C., Gadre, C. A., Gu, L., Aoki, T., Lovejoy, T. C., Dellby, N., Krivanek, O. L., Schlom, D. G., Wu, R., & Pan, X. (2021). Single-defect phonons imaged by electron microscopy. *Nature (London)*, *589*(7840), 65–69. https://doi.org/10.1038/s41586-020-03049-y

109. Cheng, Z., Li, R., Yan, X., Jernigan, G., Shi, J., Liao, M. E., Hines, N. J., Gadre, C. A., Idrobo, J. C., Lee, E., Hobart, K. D., Goorsky, M. S., Pan, X., Luo, T., & Graham, S. (2021). Experimental observation of localized interfacial phonon modes. *Nature Communications*, *12*(1), 6901. https://doi.org/10.1038/s41467-021-27250-3

110. Li, Y. H., Qi, R. S., Shi, R. C., Hu, J. N., Liu, Z. T., Sun, Y. W., Li, M. Q., Li, N., Song, C. L., Wang, L., Hao, Z. B., Luo, Y., Xue, Q. K., Ma, X. C., & Gao, P. (2022). Atomic-scale probing of heterointerface phonon bridges in nitride semiconductor. *Proceedings of the National Academy of Sciences*, *119*(8), e2117027119. https://doi.org/10.1073/pnas.2117027119

111. Haas, B., Boland, T. M., Elsässer, C., Singh, A. K., March, K., Barthel, J., Koch, C. T., & Rez, P. (2023). Atomic-resolution mapping of localized phonon modes at grain boundaries. *Nano Letters*, *23*(13), 5975–5980. https://doi.org/10.1021/acs.nanolett.3c01089

112. Hoglund, E. R., Bao, D. L., O'Hara, A., Pfeifer, T. W., Hoque, M. S. B., Makarem, S., Howe, J. M., Pantelides, S. T., Hopkins, P. E., & Hachtel, J. A. (2023). Direct visualization of localized vibrations at complex grain boundaries. *Advanced Materials*, *35*(13), 2208920. https://doi.org/10.1002/adma.202208920

113. Yan, J., Shi, R., Wei, J., Li, Y., Qi, R., Wu, M., Li, X., Feng, B., Gao, P., Shibata, N., & Ikuhara, Y. (2024). Nanoscale localized phonons at Al_2O_3 grain boundaries. *Nano Letters*, *24*(11), 3323–3330. https://doi.org/10.1021/acs.nanolett.3c04149

114. Hage, F. S., Radtke, G., Kepaptsoglou, D. M., Lazzeri, M., & Ramasse, Q. M. (2020). Single-atom vibrational spectroscopy in the scanning transmission electron microscope. *Science*, *367*(6482), 1124–1127. https://doi.org/10.1126/science.aba1136

115. Xu, M., Bao, D. L., Li, A., Gao, M., Meng, D., Li, A., Du, S., Su, G., Pennycook, S. J., Pantelides, S. T., & Zhou, W. (2023). Single-atom vibrational spectroscopy with chemical-bonding sensitivity. *Nature Materials*, *22*(5), 612–618. https://doi.org/10.1038/s41563-023-01500-9

116. Shi, R., Li, Q., Xu, X., Han, B., Zhu, R., Liu, F., Qi, R., Zhang, X., Du, J., Chen, J., Yu, D., Zhu, X., Guo, J., & Gao, P. (2024). Atomic-scale observation of localized phonons at FeSe/SrTiO$_3$ interface. *Nature Communications*, *15*(1), 3418. https://doi.org/10.1038/s41467-024-47688-5

117. Yan, X., Zeiger, P. M., Huang, Y., Sun, H., Li, J., Gadre, C. A., Yang, H., He, R., Aoki, T., Zhong, Z., Nie, Y., Wu, R., Rusz, J., & Pan, X. (2023). Real-space visualization of frequency-dependent anisotropy of atomic vibrations. *arXiv preprint arXiv:2312.01694*. https://doi.org/10.48550/arXiv.2312.01694

118. Dwyer, C. (2023). Quantum limits of transmission electron microscopy. *Physical Review Letters*, *130*(5), 056101. https://doi.org/10.1103/PhysRevLett.130.056101

How to cite this article: Bugnet, M., Löffler, S., Ederer, M., Kepaptsoglou, D. M., & Ramasse, Q. M. (2024). Current opinion on the prospect of mapping electronic orbitals in the transmission electron microscope: State of the art, challenges and perspectives. *Journal of Microscopy*, 1–19. https://doi.org/10.1111/jmi.13321